Acta Mechanica Sinica
https://doi.org/10.1007/s10409-020-00993-w

RESEARCH PAPER

Study of vertically ascending flight of a hawkmoth model

Anh Tuan Nguyen[1] · Vu Dan Thanh Le[1] · The Hung Tran[2] · V. N. Duc[3,4] · Van Binh Phung[1]

Received: 31 January 2020 / Revised: 28 May 2020 / Accepted: 14 July 2020

Abstract
This paper provides insight into the wing kinematics, the power requirement and the dynamic stability characteristics of a hawkmoth model in vertically ascending flight. The wing kinematics of the hawkmoth model is obtained based on the minimum required power assumption. The optimization process is conducted using genetic and simplex algorithms that are coupled with an artificial neural network to rapidly predict the aerodynamic force and required power. The training data for the neural network are generated from an unsteady vortex-lattice method. Compared to hover, the results in this study show the larger flapping frequency and the smaller rotation amplitude of the hawkmoth wing kinematics in ascending flight. Additionally, more power is required when the ascending speed increases. While conducting a dynamic modal analysis based on a cycle-average approach, the certain effect of the ascending speed on the modal structures of the hawkmoth model was observed.

Keywords Hawkmoth · Ascending flapping flight · Genetic algorithm · Artificial neural network · Flight dynamic stability

1 Introduction

Insect flight has recently drawn a lot of attention of researchers due to its advanced characteristics that are applicable to the future designs of flapping-wing micro air vehicles (FWMAVs). Many aspects related to the aerodynamics, flight dynamics and control problems of insect flight have been revealed in many studies [1–7]. In general, insects may conduct various flight modes, including hover, forward and vertical translations, banked turns, etc.[1, 8–10]. While hover and forward flight are regarded as basic modes that have been thoroughly investigated in many studies [11–13], research results into vertically ascending flight are still limited. However, this type of flight is very important for both biological insects and insect-like FWMAVs [10, 14].

✉ V. N. Duc
nguyenvietduc@tdtu.edu.vn

1 Faculty of Aerospace Engineering, Le Quy Don Technical University, Hanoi, Vietnam

2 Institute of Theoretical and Applied Research, Duy Tan University, Hanoi, Vietnam

3 Division of Construction Computation, Institute for Computational Science, Ton Duc Thang University, Ho Chi Minh City, Vietnam

4 Faculty of Civil Engineering, Ton Duc Thang University, Ho Chi Minh City, Vietnam

It is noteworthy that the wing motions of insects in general and those of hawkmoths in specific while hovering and in forward flight can be easily observed and recorded in wind-tunnel experiments [1, 15, 16]. Many analyses have been carried out for hawkmoths based on these measured wing kinematic data to provide lots of insight into the characteristics of hover and forward flight. For example, by tuning the kinematic data measured by Willmott and Ellington [1], Kim et al. [17] showed the effect of the forward flight speed on the natural mode structures of a hawkmoth model. Willmott and Ellington [2] and Warfvinge et al. [16] used the measured wing kinematics to estimate the required power of hawkmoths to sustain flight at various forward speeds.

Measuring the wing kinematics of hawkmoths while ascending seems to be more difficult, and no empirical data of hawkmoth in this flight mode has been published, so far. Therefore, it is troublesome for researchers to conduct ascending flight analyses. To overcome this difficulty, in this paper, we attempt to create the ascending flight wing kinematics of a hawkmoth model based on the assumption of minimum required power. In reality, hawkmoths do not fly under a minimum power condition because a small portion of energy is scarified to enhance flight stability and maneuverability [18]. However, wing kinematics at this flight condition is still quite close to that observed from actual hawkmoths

Published online: 14 September 2020

Table 1 Mass and morphological parameters of the hawkmoth

Parameters	Values
m (mg)	1578.70
R (mm)	48.50
$\bar{c}$(mm)	16.81
S (mm^2)	815.33
r_2	0.53

[19]. The wing kinematic functions of the hawkmoth model at various ascending speeds are found by integrating an artificial neural network into genetic and simplex algorithms. Analyses on the power requirement and the dynamic stability are conducted to indicate how the variation in the ascending speed affect the characteristics of hawkmoth flight. It should be noted that in this study, for the first time, the optimal wing kinematics and the important characteristics of hawkmoth ascending flight are obtained and analyzed, and these data may be useful for researchers who have an intention to carry out more studies on hawkmoth ascending flight in the future.

2 The hawkmoth model and wing kinematics definitions

In this study, we attempt to build an insect model that is as close as possible to a biological hawkmoth. The morphology and the mass distribution of the model are based on the measurement data by Ellington [20] and O'Hara and Palazotto [21]. Some basic parameters of the model, including the total mass m, the wing length R, the mean wing chord $\bar{c}$, the wing area S and the radius of the second moment of the wing area r_2 are shown in Table 1. The two wings of the hawkmoth are connected to the body by three-degree-of-freedom revolute joints. The orientations of the wings are determined by three Euler angles that are the sweep angle ϕ, the elevation angle θ and the rotation angle α. The sweep angle varies when the hawkmoth needs to move its wings for- and backward; the elevation angle is corresponding to the up- and downward motions; and the change in the rotation angle is related to the rotation of the wings about their feathering axes. The illustration of these angles are shown in Fig. 1. In this figure, β and χ denote the stroke plane and the body angles, respectively. Here, we note that according to the observation from hawkmoth flight in a wind tunnel [1], the angle between the stroke plane and the body axis is assumed constant and equals 120°. The fixed inclination of the stroke plane to the body axis has also been found in vertically ascending fruitflies and droneflies in forward flight [10, 15]. Therefore, it is relevant to state that this flight behavior is valid for many insect species in all flight modes.

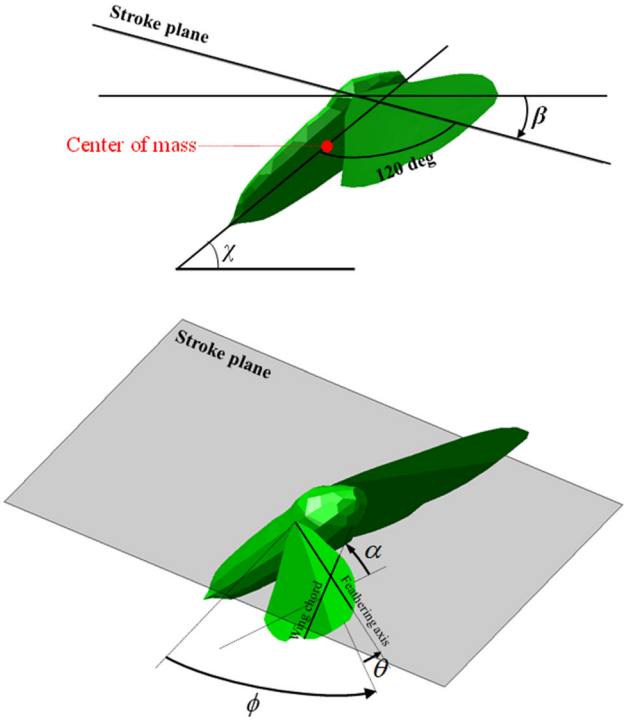

Fig. 1 Insect model and angle definitions

The time variations of the Euler angles take harmonic forms as follows:

$$\begin{aligned} \phi &= \phi_a \sin\left(2\pi f t + \frac{3\pi}{2}\right) + \phi_0, \\ \theta &= \theta_0, \\ \alpha &= \frac{\pi}{2} - \alpha_a \sin\left(2\pi f t + \frac{3\pi}{2}\right) + \alpha_0, \end{aligned} \tag{1}$$

where a and 0 respectively represent the amplitude and mean values, f is the flapping frequency. In this study, for simplicity, the variation of the elevation angle θ, which was found very small in actual hawkmoth flight, is neglected.

3 Methodology

3.1 Aerodynamic force and power prediction model

In this study, the lift, drag, pitching moment and required power are determined by an artificial-neural-network-based prediction model. According to Nguyen et al. [18], the use of artificial neural networks (ANNs) can guarantee a good accuracy level of the prediction results while the computational time is reduced substantially. Compared to conventional quasi-steady aerodynamic models [22, 23], an ANN-based models seem to be more suitable for optimization problems due to their lower computational cost and higher fidelity. An

ANN built in this study encompasses the input, output and hidden layers as shown in Fig. 2. In the input layer, there are a bias b_1 and seven kinematic variables that are the flapping frequency f, the stroke plane angle β, the mean sweep, elevation and rotation angles ϕ_0, θ_0 and α_0, and the sweep and rotation amplitudes ϕ_a and α_a. These kinematic variables are used to define the wing motions and the position of the insect model. It is noteworthy that the body angle χ can be directly determined from the stroke plane angle β based on the assumption of constant angle between the body axis and the stroke plane. The hidden layer of the ANN comprises a bias b_2 and 500 neurons. It is noted that the biases b_1 and b_2 are employed in this ANN to improve the effectiveness of the training process by enabling the transfer functions in the hidden and output layers to be shifted left or right flexibly. Sigmoid and linear transfer functions are used in the hidden and output layers, respectively. Weight sets $\boldsymbol{w}_i$ and $\boldsymbol{w}_o$ represent the strength of the connections in the ANN, and the values of these weights are updated along with the biases during the training process. The output layer includes the nondimensionalized mean lift, drag, pitching moment and required power, which are defined as

$$\begin{aligned} \overline{L}^{+} &= \frac{\overline{L}}{W}, \\ \overline{D}^{+} &= \frac{\overline{D}}{W}, \\ \overline{M}^{+} &= \frac{\overline{M}}{W\overline{c}}, \\ \overline{P}^{+} &= \frac{\overline{P}}{P_0}, \end{aligned} \tag{2}$$

where $\overline{L}$, $\overline{D}$, $\overline{M}$ and $\overline{P}$ denote the mean lift, drag, pitching moment and required power, respectively, W is the weight of the insect model, $\overline{c}$ is the mean wing chord, and $P_0 = 84.2$ mW is the required power of an actual hawkmoth in hover, which was estimated in the literature [18]. Based on the investigation result of Casey [24], the elastic storage mechanism is not applied to the present hawkmoth model. Therefore, the negative power is dissipated and not stored in the elastic elements at the joints. A more detailed description of this mechanism is given in the literature [24].

The training process of the ANN is based on a gradient-based approach that employs the Levenberg–Marquardt optimization method [25]. The training data are generated by an extended unsteady vortex-lattice method (UVLM) [26]. There are 3000 data sets for each ascending speed, and each set consists of seven input kinematic variables and four output variables as shown in Fig. 2. The input variables, which satisfy the constraints given in Table 2, are generated randomly. It should be noted that the upper and lower bounds of each kinematic variable are chosen based on the experimental data of actual hawkmoths [1] to make sure that all possible wing kinematic combinations can be considered in an optimization process. Wider ranges of these variables are unnecessary because they may result in more computational cost of the optimization process. The sweep angle amplitude ϕ_a is not allowed to exceed 60° to avoid the collision between the two wings.

To provide the training data, we employ the extended UVLM, which was developed in Nguyen et al. [26] and its validity has been confirmed in many previous studies [12, 18, 27–29]. This method is based on the potential-flow theory, which is applied to an inviscid and non-rotational

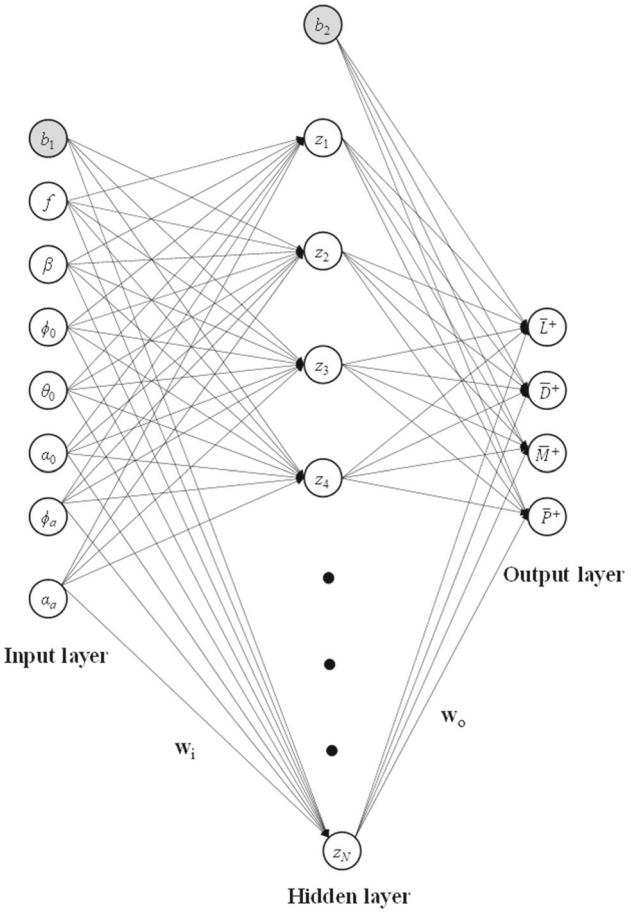

Fig. 2 Artificial neural network structure

Table 2 Mass and morphological parameters of the hawkmoth

	Min	Max
f (Hz)	15	40
β (°)	0	50
ϕ_0 (°)	− 25	25
θ_0 (°)	− 25	25
α_0 (°)	− 25	25
ϕ_a (°)	30	60
α_a (°)	25	75

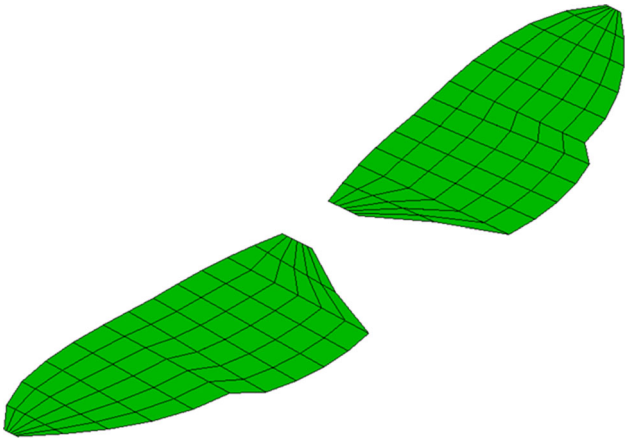

Fig. 3 Aerodynamic panels of the wings

flow. It is noteworthy that hawkmoth wings operate at large angles of attack [1] and a Reynolds number of around 10,000. According to Ellington [30], for these flight conditions, the contribution of the skin friction drag is minor and negligible. Hence, the application of the potential-flow theory, which does not include the effect of the skin friction on the wing surfaces, is relevant in this study. To enhance the accuracy of aerodynamic prediction results, Nguyen et al. [26] incorporated leading-edge suction analogy and vortex-core growth models into the UVLM. Due to these extensions, the delayed stall phenomenon occurring on insect wings [31] and the effect of the viscous diffusion [32] can be included.

When applying the extended UVLM, the wings are discretized into vortex ring panels as shown in Fig. 3. The no-penetration boundary condition is satisfied at the collocation points located at the centers of these panels. The Kutta condition is employed at the trailing edges of the wings; therefore, all vortices along these edges are shed freely to the surrounding environment to form a wake [33]. The wake geometry keeps being deformed when these vortices travel with local flow velocities. It is noteworthy that the contribution of the body aerodynamics is insignificant [12]. Thus, the aerodynamic force is generated only by the flapping wings of the hawkmoth model.

Compared to other methods, the extended UVLM has moderate computational cost and fidelity. While computational fluid dynamics (CFD) methods are too costly [34, 35], low-order methods based on the quasi-steady flow assumption [22, 23, 36] have modest fidelity given that they cannot predict the unsteady effect. In this study, thousands of data sets are required to be generated by an aerodynamic model to train the ANN for each ascending speed. Hence, considering a compromise between computational effort and fidelity, the use of the extended UVLM seems to be the most appropriate. Figure 4 shows the comparisons between the lift, drag and aerodynamic power coefficients C_L, C_D and C_P predicted by the present extended UVLM and those by other methods in the hovering case with biological wing kinematics [23]. The definitions of these coefficients are given in the literature [23]. It is seen that the results from the extended UVLM and the CFD method are close to the experimental data whereas the quasi-steady models produce the poorer predictions.

After being trained with 3000 random data sets, the ANN is used to predict the aerodynamic coefficients for other 50 random cases. The very close agreement between the predicted results by the ANN and those from the extended UVLM for hover and ascending flight as shown in Fig. 5 serves to validate the ANN model developed in this study. Nguyen et al. [26] found that compared to the direct use of the extended UVLM, ANNs can increase the prediction speed by thousands of times.

3.2 Optimization method

As mentioned earlier in this paper, the wing kinematics of the hawkmoth model is found based on the minimum required power assumption. Based on the result observed by Willmott and Ellington [1] from biological hawkmoth flight, the oscillation of the body can be neglected. To satisfy the equilibrium condition, the mean drag force and pitching moment are zero and the mean lift force equals the total weight of the model. Similar to the literature [18], the fitness function used in this study is as below:

$$F = \overline{P}^{+} + r\left(\left|1 - \overline{L}^{+}\right| + \left|\overline{D}^{+}\right| + \left|\overline{M}^{+}\right|\right) + s\sum_{i=1}^{7}\frac{|\zeta_i|}{\mathrm{Max}_i - \mathrm{Min}_i}, \tag{3}$$

where r and s are positive real parameters specifying the strength of the penalty for violating the constraints. According to Nguyen et al. [18], r and s are set to 2.0 and 5.0, respectively. ζ_i is the distance by which parameter i is outside the range given in Table 2. The nondimensionalized mean lift, drag, pitching moment and required power $\overline{L}^{+}$, $\overline{D}^{+}$, $\overline{M}^{+}$ and $\overline{P}^{+}$ in Eq. (3) are provided by the ANN.

The optimization method employed here is developed by combining genetic and simplex algorithms to obtain the minimum value of the fitness function. First, the genetic algorithm (GA) is used to obtain the globally minimal basin. Next, the locally optimal solution of the basin is found by the simplex algorithm based on the Nelder-Mead method [37]. The GA is inspired by the process of natural evolution and relies on bio-inspired operators such as mutation, crossover and selection [38]. For each generation, the program creates a large population, and each individual of the population contains a seven-chromosome gene that corresponds to seven input parameters shown in Fig. 2. The top 5% of the population with the best fitness values are regarded as elite individuals and survive to the next generation. For the remaining indi-

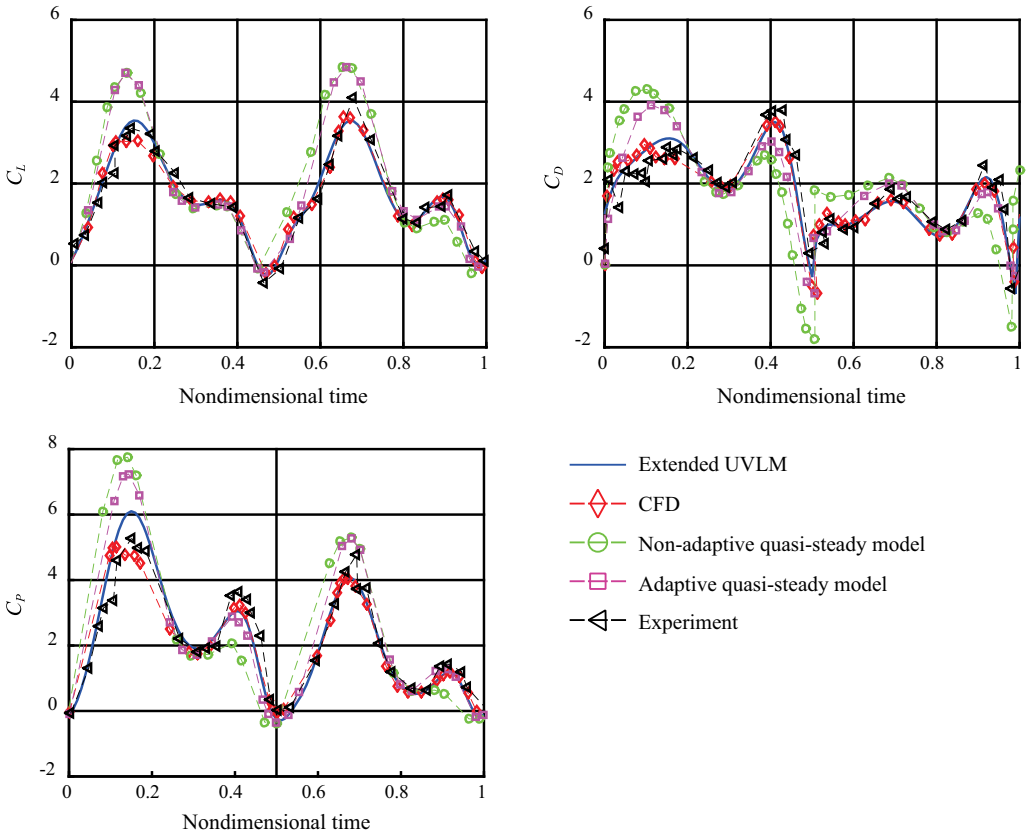

Fig. 4 Aerodynamic coefficients in the hovering case predicted by various methods

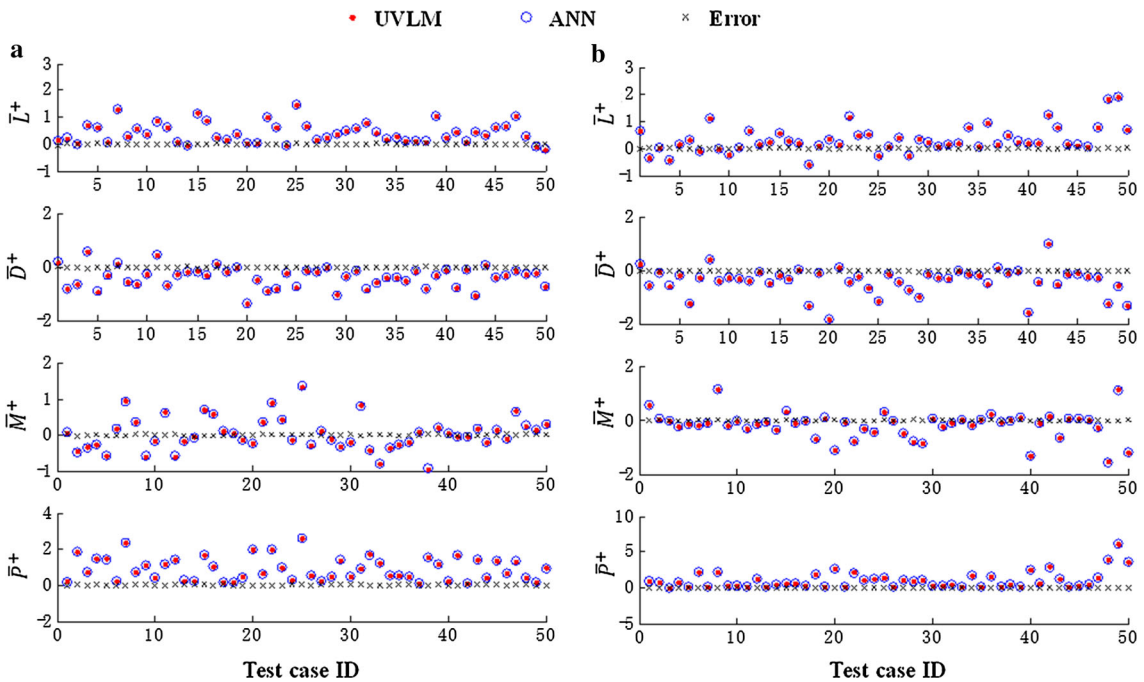

Fig. 5 Nondimensionalized mean lift, drag, pitching moment and aerodynamic power predicted by the ANN and the extended UVLM for hover (**a**) and ascending flight at 1.0 m/s (**b**)

viduals, the mutation and crossover operators are applied to produce new individuals. Based on the convergence analysis results in the literature [18], a population size of 10^5 is chosen in this study. For the present problem, the tolerance of the fitness function F is set to be 10^{-6} and 10^{-10} for the GA and the simplex algorithms, respectively.

The validation of the present ANN-based optimization method was confirmed in the literature [18] for the same hawkmoth model in hover. In this study, this method is applied to the hawkmoth model in both hover and vertically ascending flight.

3.3 Equations of motion and their linearized form

Zhang and Sun [39] have derived the nonlinear six-degree-of-freedom equations of motion for insect flapping flight as follows:

$$ {}_b\mathbf{F}_A + m_b\mathbf{g} = m({}_b\dot{\mathbf{V}}_{cg} + {}_b\boldsymbol{\omega}_{bd} \times {}_b\mathbf{V}_{cg}) + \mathbf{a}_1 + \mathbf{b}_1, \tag{4} $$

$$ \begin{aligned} {}_b\mathbf{M}_A + \sum_{i=1}^{2} \left[m_{wg} \left({}_b\mathbf{R}_h + {}_b\mathbf{R}_{wg} \right) \times {}_b\mathbf{g} \right]_i &= {}_b\boldsymbol{\omega}_{bd} \\ \times ({}_b\mathbf{I}_{bd} + \mathbf{c}_2)_b\boldsymbol{\omega}_{bd} + ({}_b\mathbf{I}_{bd} + \mathbf{c}_2)_b\dot{\boldsymbol{\omega}}_{bd} + \mathbf{a}_2 + \mathbf{b}_2, \end{aligned} \tag{5} $$

where ${}_b\boldsymbol{F}_A$ and ${}_b\boldsymbol{M}_A$ are the total aerodynamic force and moment about the body center of mass, m and m_{wg} are the total mass of the insect model and the mass of its wing, respectively, ${}_b\boldsymbol{g}$ denotes the gravitational acceleration, ${}_b\boldsymbol{I}_{bd}$ is the moment of inertia tensor of the body, ${}_b\boldsymbol{V}_{cg}$ is the velocity of the body center of mass, ${}_b\boldsymbol{\omega}_{bd}$ is the angular velocity of the body, and ${}_b\boldsymbol{R}_h$ and ${}_b\boldsymbol{R}_{wg}$ are the vectors from the body center of mass to the root of a wing and from this wing root to the wing center of mass. The subscript b represents the body-fixed coordinate system (Fig. 6) while $\boldsymbol{a}_1$, $\boldsymbol{a}_2$, $\boldsymbol{b}_1$, $\boldsymbol{b}_2$ and $\boldsymbol{c}_2$ denote terms related to the mass, moment of inertia and flapping motion of the wings.

To analyze the dynamic stability characteristics of insect flight, the linearized form of the equations of motion is normally used. The linearization process is applicable to a system that undergoes small disturbed motions from the equilibrium state while neglecting the contributions of high-order terms. In this case, we apply the wingbeat-cycle-average technique [5, 39, 40], which considers only the wingbeat-cycle-average values of the aerodynamic and inertial forces and moment. Hence, the fast-time-scale dynamics related to the flapping motion of the wings are ignored. The equations of motion are then simplified as [17, 41].

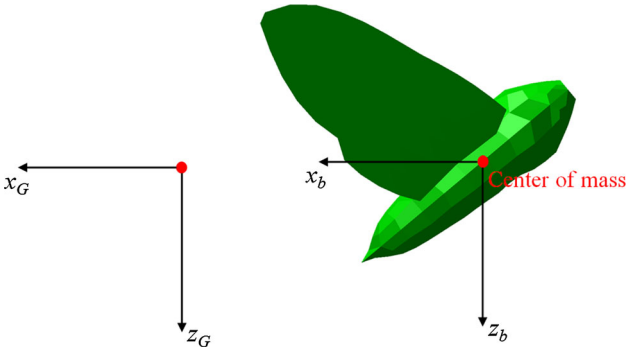

Fig. 6 Hawkmoth model with the body-fixed coordinate system x_b y_b z_b and ground-fixed coordinate system x_G y_G z_G

$$ \begin{aligned} \delta\dot{u}^+ &= \frac{X_u^+\delta u^+}{m^+} + \frac{X_w^+\delta w^+}{m^+} + \frac{X_q^+\delta q^+}{m^+} - w_e^+\delta q^+ - g^+\delta\Theta, \\ \delta\dot{w}^+ &= \frac{Z_u^+\delta u^+}{m^+} + \frac{Z_w^+\delta w^+}{m^+} + \frac{Z_q^+\delta q^+}{m^+}, \\ \delta\dot{q}^+ &= \frac{M_u^+\delta u^+}{I_y^+} + \frac{M_w^+\delta w^+}{I_y^+} + \frac{M_q^+\delta q^+}{I_y^+}, \\ \delta\dot{\Theta} &= \delta q^+, \end{aligned} \tag{6} $$

$$ \begin{aligned} \delta\dot{v}^+ &= \tfrac{Y_v^+\delta v}{m^+} + \tfrac{Y_p^+\delta p}{m^+} + \tfrac{Y_r^+\delta r}{m^+} + w_e^+\delta p + g^+\delta\Psi, \\ \delta\dot{p}^+ &= \frac{I_z^+}{I_x^+I_z^+ - I_{xz}^{+2}}\left(L_v^+\delta v^+ + L_p^+\delta p^+ + L_r^+\delta r^+\right) \\ &\quad + \frac{I_{xz}^+}{I_x^+I_z^+ - I_{xz}^{+2}}\left(N_v^+\delta v^+ + N_p^+\delta p^+ + N_r^+\delta r^+\right), \\ \delta\dot{r}^+ &= \frac{I_{xz}^+}{I_x^+I_z^+ - I_{xz}^{+2}}\left(L_v^+\delta v^+ + L_p^+\delta p^+ + L_r^+\delta r^+\right) \\ &\quad + \frac{I_x^+}{I_x^+I_z^+ - I_{xz}^{+2}}\left(L_v^+\delta v^+ + L_p^+\delta p^+ + L_r^+\delta r^+\right), \\ \delta\dot{\Psi} &= \delta p^+. \end{aligned} \tag{7} $$

In the above equations, δ denotes the small disturbance value; u, v, and w are the velocity components along the x_b-, y_b- and z_b-axes of the body-fixed coordinate system (Fig. 6); p, q, and r represent the angular velocities about these axes; m and I respectively denote the mass and the moment of inertia of the hawkmoth model; the aerodynamic forces and moments are denoted by X, Y, and Z and L, M, and N, respectively; g is the gravitational acceleration; w_e is the vertical velocity of the undisturbed model; Θ and Ψ are respectively the second and third Euler angles of the 3-2-1 sequence of rotations to define the orientation of the body-fixed frame relative to the ground-fixed frame. These two frames coincide with each other when Θ and Ψ are zero (Fig. 6). The superscript " + " denotes nondimensionalized variables that are defined as follows:

$$
\begin{aligned}
&m^+ = \frac{m}{0.5\rho U S_t T}, \quad g^+ = \frac{gT}{U}, \quad t^+ = \frac{t}{T},\\
&I_x^+ = \frac{I_x}{0.5\rho U^2 S_t \bar{c} T^2}, \quad I_y^+ = \frac{I_y}{0.5\rho U^2 S_t \bar{c} T^2},\\
&I_z^+ = \frac{I_z}{0.5\rho U^2 S_t \bar{c} T^2}, \quad I_{xz}^+ = \frac{I_{xz}}{0.5\rho U^2 S_t \bar{c} T^2},\\
&\delta u^+ = \frac{\delta u}{U}, \quad \delta v^+ = \frac{\delta v}{U}, \quad \delta w^+ = \frac{\delta w}{U}, \quad \delta p^+ = \delta p T,\\
&\delta q^+ = \delta q T, \quad \delta r^+ = \delta r T,\\
&X^+ = \frac{X}{0.5\rho U^2 S_t}, \quad Y^+ = \frac{Y}{0.5\rho U^2 S_t}, \quad Z^+ = \frac{Z}{0.5\rho U^2 S_t},\\
&L^+ = \frac{L}{0.5\rho U^2 S_t \bar{c}}, \quad M^+ = \frac{M}{0.5\rho U^2 S_t \bar{c}}, \quad N^+ = \frac{N}{0.5\rho U^2 S_t \bar{c}},
\end{aligned}
\tag{8}
$$

where ρ is the air density, S_t is the total area of the two wings, T is the wingbeat stroke cycle, and U is the mean wing velocity defined by $2\phi_a f r_2$.

Equations 6 and 7 can be expressed in the following form:

$$
\begin{bmatrix} \delta\dot{u}^+ \\ \delta\dot{w}^+ \\ \delta\dot{q}^+ \\ \delta\dot{\Theta} \end{bmatrix} = \boldsymbol{A}_{long}^+ \begin{bmatrix} \delta u^+ \\ \delta w^+ \\ \delta q^+ \\ \delta\Theta \end{bmatrix}, \tag{9}
$$

$$
\begin{bmatrix} \delta\dot{v}^+ \\ \delta\dot{p}^+ \\ \delta\dot{r}^+ \\ \delta\dot{\Psi} \end{bmatrix} = \boldsymbol{A}_{lat}^+ \begin{bmatrix} \delta v^+ \\ \delta p^+ \\ \delta r^+ \\ \delta\Psi \end{bmatrix}, \tag{10}
$$

where

$$
\boldsymbol{A}_{long}^+ = \begin{bmatrix} \frac{X_u^+}{m^+} & \frac{X_w^+}{m^+} & \frac{X_q^+}{m^+} - w_e^+ & -g^+ \\ \frac{Z_u^+}{m^+} & \frac{Z_w^+}{m^+} & \frac{Z_q^+}{m^+} & 0 \\ \frac{M_u^+}{I_y^+} & \frac{M_w^+}{I_y^+} & \frac{M_q^+}{I_y^+} & 0 \\ 0 & 0 & 1 & 0 \end{bmatrix}, \tag{11}
$$

$$
\boldsymbol{A_{lat}}^+ = \begin{bmatrix} \frac{Y_v^+}{m^+} & \frac{Y_p^+}{m^+} + w_e^+ & \frac{Y_r^+}{m^+} & g^+ \\ \frac{I_z^+ L_v^+ + I_{xz}^+ N_v^+}{I_x^+ I_z^+ - I_{xz}^{+\,2}} & \frac{I_z^+ L_p^+ + I_{xz}^+ N_p^+}{I_x^+ I_z^+ - I_{xz}^{+\,2}} & \frac{I_z^+ L_r^+ + I_{xz}^+ N_r^+}{I_x^+ I_z^+ - I_{xz}^{+\,2}} & 0 \\ \frac{I_{xz}^+ L_v^+ + I_x^+ N_v^+}{I_x^+ I_z^+ - I_{xz}^{+\,2}} & \frac{I_{xz}^+ L_p^+ + I_x^+ N_p^+}{I_x^+ I_z^+ - I_{xz}^{+\,2}} & \frac{I_{xz}^+ L_r^+ + I_x^+ N_r^+}{I_x^+ I_z^+ - I_{xz}^{+\,2}} & 0 \\ 0 & 1 & 0 & 0 \end{bmatrix}. \tag{12}
$$

After obtaining the wing kinematics of the hawkmoth model at the equilibrium state, the stability derivatives that appear in the expressions of $\boldsymbol{A}_{long}^+$ and $\boldsymbol{A}_{lat}^+$ (Eqs. (11) and (12)) are determined by the extended UVLM. It is important to note that Eqs. (9) and (10) are corresponding to the longitudinal and lateral motions of the model, respectively.

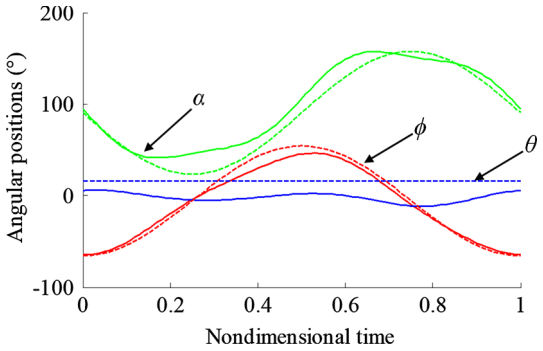

Fig. 7 Optimal (dashed lines) and biological (solid lines) wing kinematics [1]

Therefore, by obtaining the eigenvalues and eigenvectors of $\boldsymbol{A}_{long}^+$ and $\boldsymbol{A}_{lat}^+$ matrices, we can respectively gain insight into the longitudinal and lateral dynamic stability characteristics of the present hawkmoth model while ascending vertically at a constant speed.

4 Results and discussion

4.1 Validation of the methodology

To validate the optimization approach presented in Sect. 3, the obtained hovering wing kinematic functions are compared with those of an actual hawkmoth (Fig. 7). Here, the time is nondimensionalized by the wingbeat stroke cycle. The optimal wing kinematics is represented by the dashed lines while the solid lines are corresponding to the experimental data measured from the hovering flight of an actual hawkmoth [1]. The close agreement between the two results, which is seen in Fig. 7, serves to validate the present approach used to obtain the wing kinematics of the hawkmoth model. It should be noted that the optimal elevation angle θ is just above the value of the actual hawkmoth. Nguyen et al. [18] stated that this minor difference is due to the added rotation effect [42] that helps increase the efficiency of insect flight. However, an actual hawkmoth in wild may scarify energy to improve its body pitch stability by slightly reducing the elevation angle as shown in Fig. 7.

Next, we compute the stability derivative coefficients of the longitudinal and lateral dynamic systems, which are represented by Eqs. (6) and (7). These coefficients are then used to determine the eigenvalues of matrices $\boldsymbol{A}_{long}^+$ and $\boldsymbol{A}_{lat}^+$ (Eqs. (11) and (12)). Figure 8 shows the comparisons between the eigenvalues obtained in this study and those by Cheng and Deng [43] for hovering hawkmoths. The similarity between the two sets of results can be seen in Fig. 8. For the longitudinal system, there are an unstable oscillatory mode and two stable subsidence modes whereas a marginally unstable

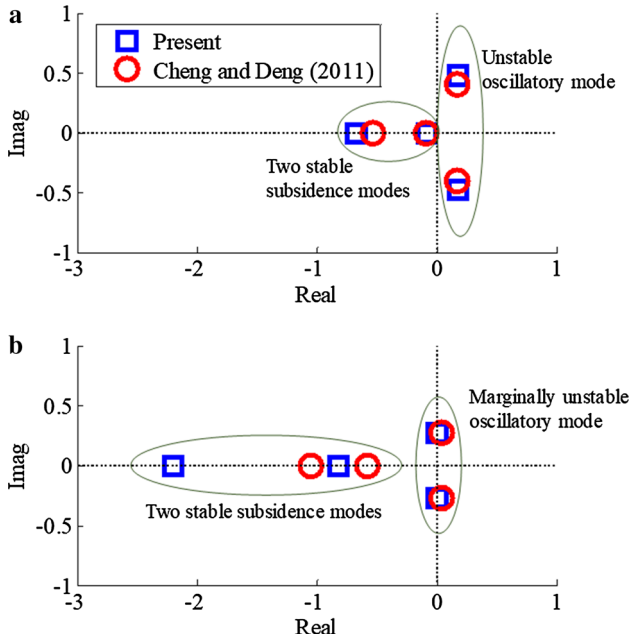

Fig. 8 Eigenvalues of the longitudinal (**a**) and lateral (**b**) dynamic systems obtained in this study and by Cheng and Deng [43]

oscillatory mode and two stable subsidence modes occur in the lateral system. It should be noted that the morphology and mass parameters of the two models used in the comparison are not from the same insect individual; therefore, some quantitative differences are observed in Fig. 8. However, the two models show the close flight dynamic stability characteristics, and this agreement can be used to validate the present method.

4.2 Effect of the ascending speed on the equilibrium flight conditions

At the equilibrium state, the resultant force and the pitch moment must be zero. Using the approach presented in Sects. 3.1 and 3.2, the wing kinematics of the hawkmoth model at several ascending speeds are obtained and given in Table 3. Figure 9 illustrates the variations of the Euler angles within the time course of one wingbeat stroke cycle.

According to the results shown in Table 3, we found that for all ascending speeds, in the optimal flight conditions, the stroke plane is almost horizontal, which is represented by a small value of β. The variation of the body angle χ appears to be very small when the ascending speed increases. The trends of the stroke plane and the body angles are similar to those observed in vertically ascending flight of fruitflies [10]. Moreover, the sweep amplitude ϕ_a reaches its maximum allowed value of 60°, and the elevation angle θ_0 is found slightly above zero (around 15°) to enhance the flight efficiency via the added rotation effect [42]. In fact, these trends have been observed while analyzing optimal hovering

Table 3 Wing kinematics at several ascending speeds

	Ascending speed (m/s)				
	0	0.5	1.0	1.5	2.0
f (Hz)	26.5	27.9	29.4	30.2	31.0
β (°)	1.5	2.2	2.8	0.6	2.9
ϕ_0 (°)	− 5.5	− 5.2	− 4.7	− 4.1	− 4.8
θ_0 (°)	15.8	14.0	15.0	14.6	14.8
α_0 (°)	0.7	1.0	1.2	0.1	1.3
ϕ_a (°)	60.0	60.0	60.0	60.0	60.0
α_a (°)	66.9	66.5	65.0	61.0	57.1
χ (°)	58.5	57.8	57.2	59.4	57.1

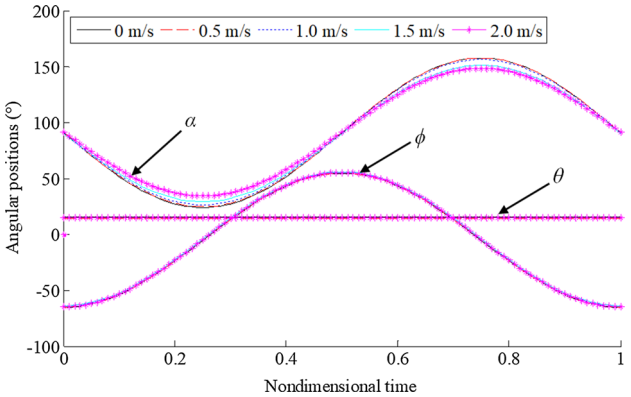

Fig. 9 Wing kinematic functions at various ascending speeds

flight of hawkmoths [18]. However, in this paper, they are proved to be valid even for vertically ascending flight at various speeds. In addition, the flapping frequency f is found to increase with the ascending speed while the rotation amplitude α_a decreases (Fig. 9). For ascending flight, a downward inflow has a negative effect on the lift production mechanism. To overcome this problem, a larger flapping frequency f is required. Moreover, by decreasing the rotation amplitude α_a, the hawkmoth model can reduce the projected area of the wings on the horizontal plane, therefore, reduce the effect of the downward inflow (Fig. 10). These trends of the flapping frequency and the rotation amplitude have been observed in vertically ascending flight of fruitflies by Shen et al. [10].

To validate the obtained equilibrium flight conditions, the nondimensionalized lift, drag, pitch moment and required power $\overline{L}^+$, $\overline{D}^+$, $\overline{M}^+$ and $\overline{P}^+$ are computed by the extended UVLM are compared with those by the ANN (Table 4). The values from the ANN are given in parentheses. We can see good agreement between the predicted values by the ANN and the exact values that are obtained from the UVLM. Only minor differences between the results in the lift and power are found in the hovering flight mode. It should be noted that in the case of hovering flight, wing-wake interaction is

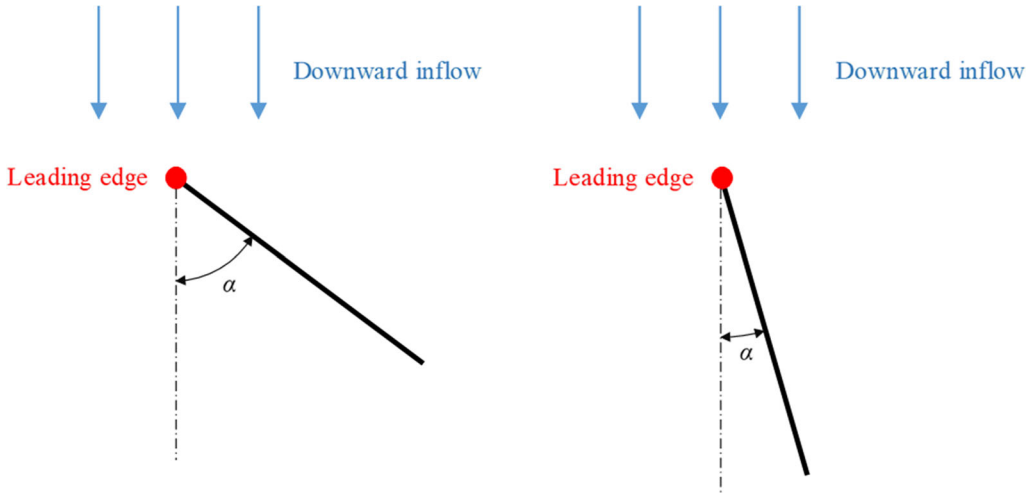

Fig. 10 Illustration of insect wings with larger (the left wing) and smaller (the right wing) rotation angles in a downward inflow condition

stronger [26, 44], which affects the quality of ANN-based predictions.

Figure 11 shows the lift and drag forces at various ascending speeds from 0 to 2.0 m/s. We can observe that at the beginning of each half stroke, the lift curve shows a minor peak, and this peak is attenuated when the ascending speed grows. These peaks are related to a strong added-mass effect that is caused by a large rotation amplitude α_a when the hawkmoth model hovers or ascends slowly [22]. Moreover, a wake capture effect may also account for the presence of these peaks [45]. At a large ascending speed, due to the stronger downward inflow, wing-wake interactions become less considerable (Fig. 12); therefore, this effect decreases. From Fig. 11, it is seen that the peak-to-peak amplitude of the drag force increases with the ascending speed. This trend is caused by a larger flapping frequency and a smaller rotation amplitude when the hawkmoth model ascends faster. It should be noted that a smaller rotation amplitude leads to a larger angle of attack, then a more significant drag force.

As shown in Table 4, more power is required at a more rapid ascent. In fact, for a larger ascending speed, the downward inflow is more severe; and thus, more power is required to overcome its negative effect (Fig. 13a). Figure 13b shows the power distribution within one wingbeat stroke cycle.

Similarly, the energy consumed per unit distance is computed and shown in Fig. 14. It is noted that the velocity due to the oscillation of the body is neglected here. Nguyen et al. [12] found that the body of a hawkmoth oscillates slightly at a velocity of below 0.1 m/s, which is much smaller than the ascending speeds considered in this paper. Interestingly, in contrast to the required power, ascending over the same distance at a larger speed is more profitable in terms of energy. In other words, despite of a higher level of power requirement, ascending faster can save more energy. However, due to the limitations in the maximum required power and the

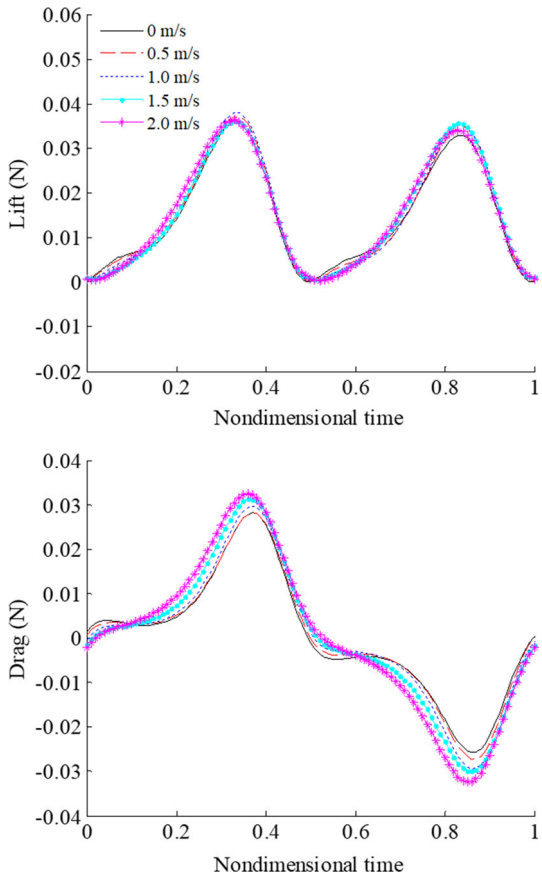

Fig. 11 Lift and drag forces at various ascending speeds

flapping frequency, there could be an upper bound of the ascending speed for each insect species. Figure 13 shows that the required mean power increases almost linearly against the ascending speed while the trend of the mean energy per unit distance follows a hyperbola as indicated in Fig. 14. In

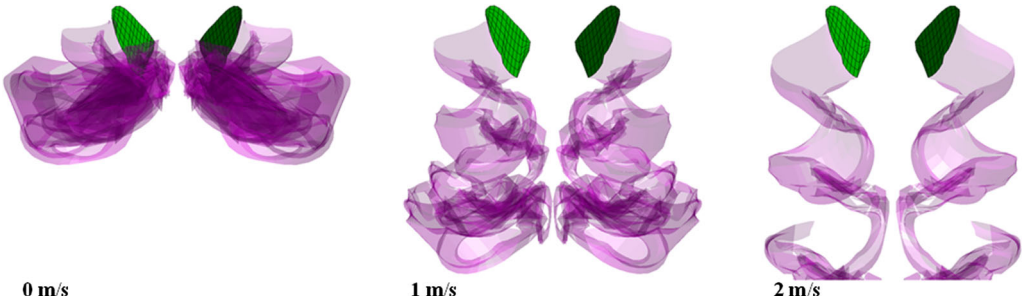

Fig. 12 Wake patterns at various ascending speeds

Table 4 Nondimensionalized lift, drag, pitch moment and required power by the ANN and UVLM at different ascending speeds

	Ascending speed (m/s)				
	0	0.5	1.0	1.5	2.0
$\overline{L}^+$	0.97 (1.0)	0.98 (1.0)	0.99 (1.0)	0.99	0.99 (1.0)
$\overline{D}^+$	0 (0)	0 (0)	0 (0)	0 (0)	0 (0)
$\overline{M}^+$	0 (0)	− 0.01 (0)	0 (0)	0 (0)	0 (0)
$\overline{P}^+$	0.86 (0.84)	0.96 (0.96)	1.09 (1.10)	1.21 (1.21)	1.34 (1.34)

specific, the mean power $\overline{P}$ and the mean energy per unit distance $\overline{E}$ follow the relationships with the ascending speed V as

$$\overline{P} = 0.0702 + 0.0215\,V, \tag{13}$$

$$\overline{E} = 0.0702\,V^{-1} + 0.0215. \tag{14}$$

4.3 Effect of the ascending speed on the dynamic stability characteristics

Figure 15 shows the movements of the eigenvalues of the longitudinal and lateral dynamic systems with an increase of the ascending speed from 0 (the hovering case) to 2.0 m/s. The imaginary part of an eigenvalue represents the nondimensional frequency of the corresponding oscillatory natural mode while the real part is used to measure the stability of this mode. A more negative value of the real part implies that disturbances related to the natural mode decay more rapidly and the dynamic system comes back to its equilibrium state more easily. On the contrary, an eigenvalue with the positive real part corresponds to an unstable natural mode. Figure 15a shows that the longitudinal dynamic system is unstable for all speeds ranging from 0 to 2.0 m/s. The arrows in this figure indicate the movement directions of the eigenvalues when the ascending speed increases. When this speed is below 1.5 m/s, there are two stable subsidence

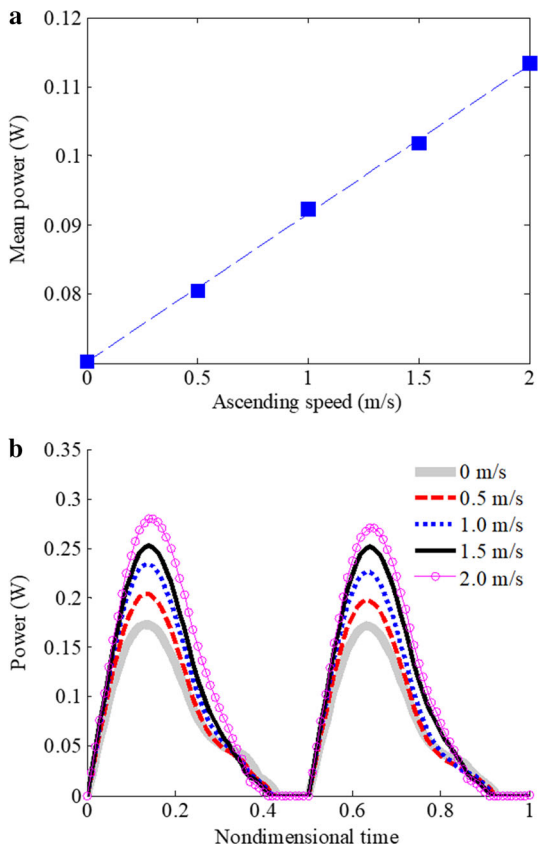

Fig. 13 Mean required power against the ascending speed with its best fit (**a**) and its distribution within one wingbeat stroke cycle (**b**)

modes and an unstable oscillatory mode. As the ascending speed increases, the eigenvalue corresponding to the unstable oscillatory mode moves toward the horizontal axis; and from 1.5 m/s, this mode becomes two separate unstable nonoscillatory modes as shown in Fig. 15a. While the slow subsidence mode appears to be independent of the ascending speed, the eigenvalue of the fast subsidence mode moves leftward when the hawkmoth model ascends faster, which signifies the better stability.

Similar to the longitudinal dynamic system, the lateral system also experiences some apparent trends of the eigen-

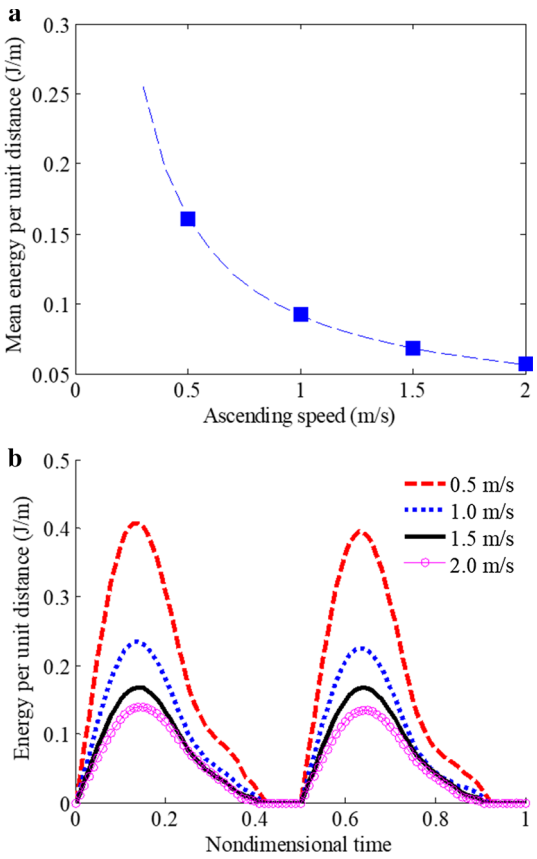

Fig. 14 Mean consumed energy per unit distance against the ascending speed with its best fit (**a**) and its distribution within one wingbeat stroke cycle (**b**)

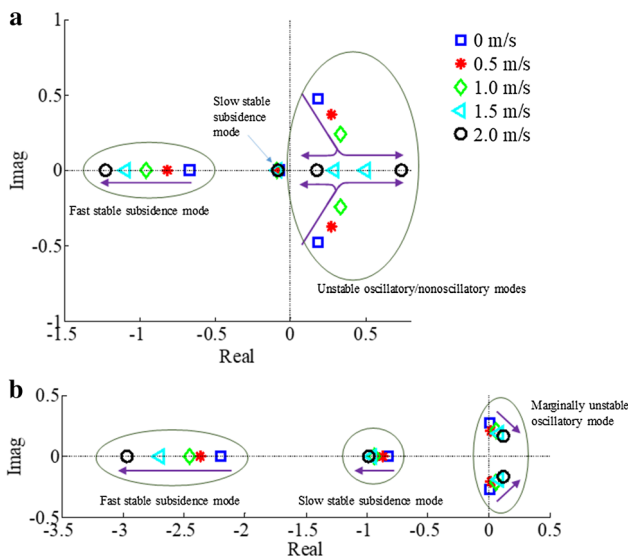

Fig. 15 Movements of the longitudinal (**a**) and lateral (**b**) eigenvalues with an increase of the ascending speed from 0 to 2.0 m/s

value movements. While hovering and ascending at a low speed, the lateral system is marginally unstable given that two stable subsidence modes and a marginally unstable oscillatory mode. However, at high speeds, the marginally unstable oscillatory mode becomes more unstable and moves toward the horizontal axis. At the same time, the stability of the two subsidence modes is augmented when the ascending speed increases.

Based on the movements of the eigenvalues as shown in Fig. 15, it is possible to state that the stable modes of the dynamic system tend to become more stable while the unstable modes become more unstable with an increase of the ascending speed. Moreover, the oscillation of the dynamic system is weakened due to the decreases of the imaginary parts.

To provide detailed explanations for the movement trends observed in Fig. 15, the variations of aerodynamic forces and moments against small disturbances are presented in Fig. 16. To use the UVLM to calculate the aerodynamic forces and moments under a disturbed condition, the velocity component arising from the corresponding disturbance is added to the expression of the no-penetration boundary condition at each collocation point as follows:

$$\left(\boldsymbol{V}_{ib} + \boldsymbol{V}_{iw} - \boldsymbol{V}_{w/eq} - \boldsymbol{V}_{w/d}\right) \cdot \boldsymbol{n} = 0, \tag{15}$$

where $\boldsymbol{V}_{ib}$ and $\boldsymbol{V}_{iw}$ are the velocity induced by the bound vortices on the wings and that by the wake, respectively, $\boldsymbol{V}_{w/eq}$ denotes the velocity of the wing in the equilibrium condition, $\boldsymbol{V}_{w/d}$ is the disturbance velocity added to the model, and $\boldsymbol{n}$ denotes the normal velocity of the wing surface.

From the plots in Fig. 16a, we found that the ascending speed has very little influences on the longitudinal stability derivative coefficients. Therefore, it is possible to state that the movement trends of the longitudinal eigenvalues are primarily attributed to the vertical velocity term w_e^+ in Eq. 11. To validate this statement, a new matrix $\boldsymbol{A}_{long}^+$ is built with the term w_e^+ varying within a range corresponding to the ascending speed from 0 to 2.0 m/s while the stability derivative coefficients are held unchanged and independent of the ascending speed. Figures 17a–e show the longitudinal eigenvalues of the new matrix $\boldsymbol{A}_{long}^+$ with the stability derivative coefficients taken from ascending flight states at 0 m/s, 0.5 m/s, 1.0 m/s, 1.5 m/s and 2.0 m/s, respectively. It is seen that the movement trends of the eigenvalues in these figures are the same, which means the differences in the longitudinal stability derivatives as shown in Fig. 16a are so small that they do not have any substantial effect on the structure of the longitudinal dynamic system. The movements of the eigenvalues exhibited in Fig. 15a mainly come from the variation of the vertical velocity, which is represented by w_e^+ in Eq. (11).

Similarly, a new lateral matrix $\boldsymbol{A}_{lat}^+$ from Eq. (12) is derived with the lateral stability derivative coefficients taken from ascending flight states at 0 m/s, 0.5 m/s, 1.0 m/s, 1.5 m/s and 2.0 m/s (Fig. 18). It is found that the movement trends

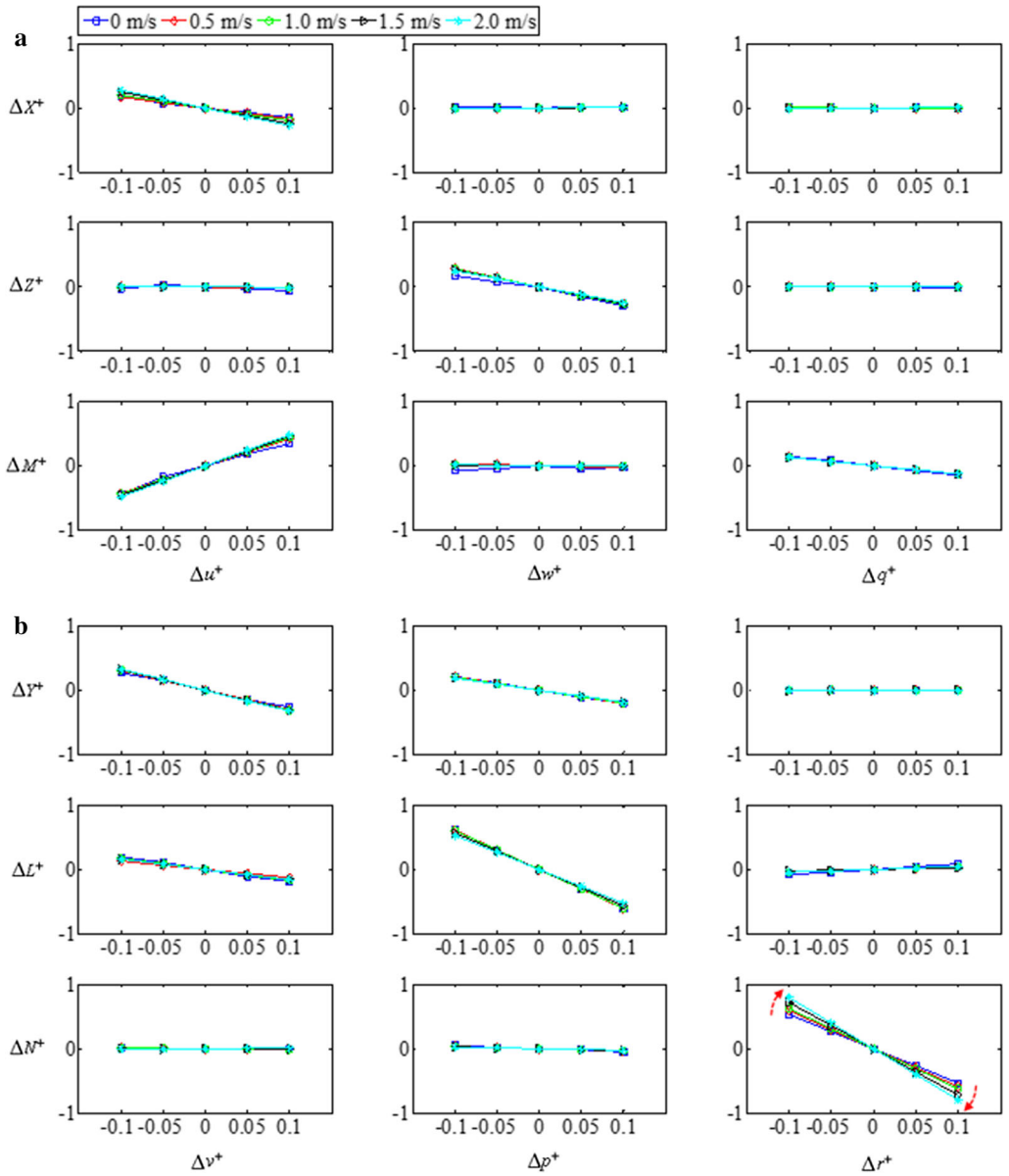

Fig. 16 Stability derivatives at various ascending speeds for the longitudinal (**a**) and lateral (**b**) dynamic systems

of the unstable oscillatory and the slow subsidence modes are basically the same as those observed in Fig. 15b. However, no certain movement of the eigenvalue corresponding to the fast subsidence mode is seen in Fig. 18. Unlike the longitudinal stability derivatives, for the lateral system, the coefficient N_r^+ is profoundly affected by the ascending speed (Fig. 16b). The variation of this coefficient with an increase of the ascending speed may account for the leftward movement of the fast subsidence mode. To validate this statement, let N_r^+ vary with the ascending speed while other stability derivative coefficients are taken from the hovering case and held constant, then the eigenvalue plot in Fig. 18a turns to that in Fig. 19. The trends of the eigenvalues in Fig. 19 are very similar to those in Fig. 15b. Hence, it is relevant to state that the variation of N_r^+ has a great effect on the movement trend of the fast subsidence mode of the lateral dynamic system. To explain the influence of the ascending speed on the value of N_r^+, we should firstly understand N_r^+ as the damping coefficient corresponding to the rotation of the model about the z_b axis. As mentioned earlier, as the ascending speed increases, the reduction in the rotation angle will cause larger wing drag as shown in Fig. 11. Consequently, the larger value of N_r^+ is achieved at a faster ascent as indicated by Fig. 16b. Here, it is noteworthy that the movements of the unstable oscillatory and the slow subsidence modes are simply due to the variation of the term w_e^+ in the expression of $\boldsymbol{A}_{lat}^+$ in Eq. (12).

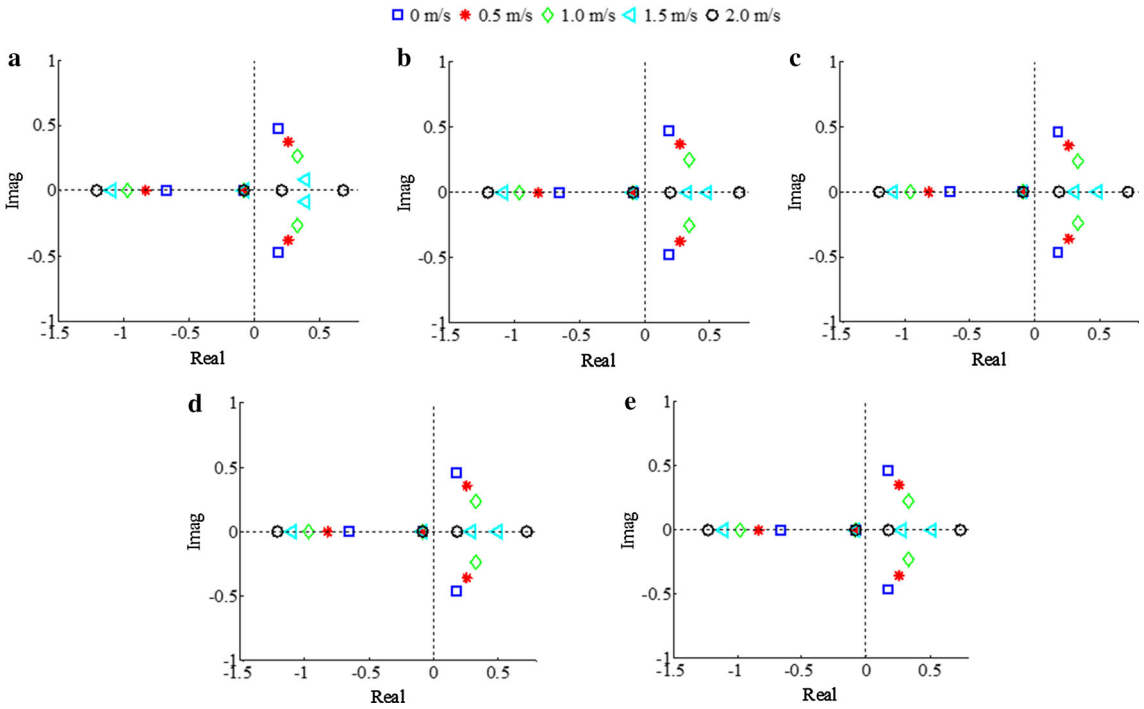

Fig. 17 Longitudinal eigenvalues with the stability derivative coefficients taken from ascending flight states at 0 m/s (**a**), 0.5 m/s (**b**), 1.0 m/s (**c**), 1.5 m/s (**d**) and 2.0 m/s (**e**)

5 Conclusions

In this paper, we have obtained the wing kinematics of a hawkmoth model in vertically ascending flight based on the assumption of minimum required power. The optimization process is conducted by integrating an artificial neural network (ANN) into genetic and simplex algorithms. The training data of the ANN are provided by the extended unsteady vortex-lattice method. The results show that with an increase of the ascending speed, the flapping frequency grows while the rotation amplitude decreases. More power is required when the hawkmoth model ascends faster. However, in terms of energy consumption per unit travelled distance, ascending at a higher speed is more advantageous. While studying the dynamic stability characteristics of the model, it is found that for all considered ascending speeds from 0 to 2.0 m/s, our dynamic system is unstable. The certain trends of the eigenvalue movements are observed in this study. In general, we can state that unstable modes tend to be more unstable whereas stable modes become more stable as the ascending speed increases. We also found that the damping coefficient corresponding to the rotation of the model about the vertical axis varies greatly with the ascending speed, and this variation causes the fast subsidence mode of the lateral dynamic system to be more stable.

For actual hawkmoths, it seems that no recorded data from vertically ascending flight have been published. The variation trend of the wing kinematic parameters against the ascending speed obtained in this paper shows some agreements with that of actual fruitflies, especially in terms of flapping frequency, stroke plane orientation, and body and wing pitch angles. However, in reality, hawkmoths may not always fly under the energy-optimal condition; therefore, more empirical data regarding hawkmoth ascending flight are required to rigorously validate the present results. Despite of this fact, the numerical data of the wing kinematics, power requirement and dynamic stability characteristics, which are mentioned for the first time in this paper, imply that there could be a lot of interesting physical aspects that actual hawkmoths may experience in vertically ascending flight and may not be observed in any other flight modes. As for bio-inspired FWMAVs, the findings in this work could be helpful for the development

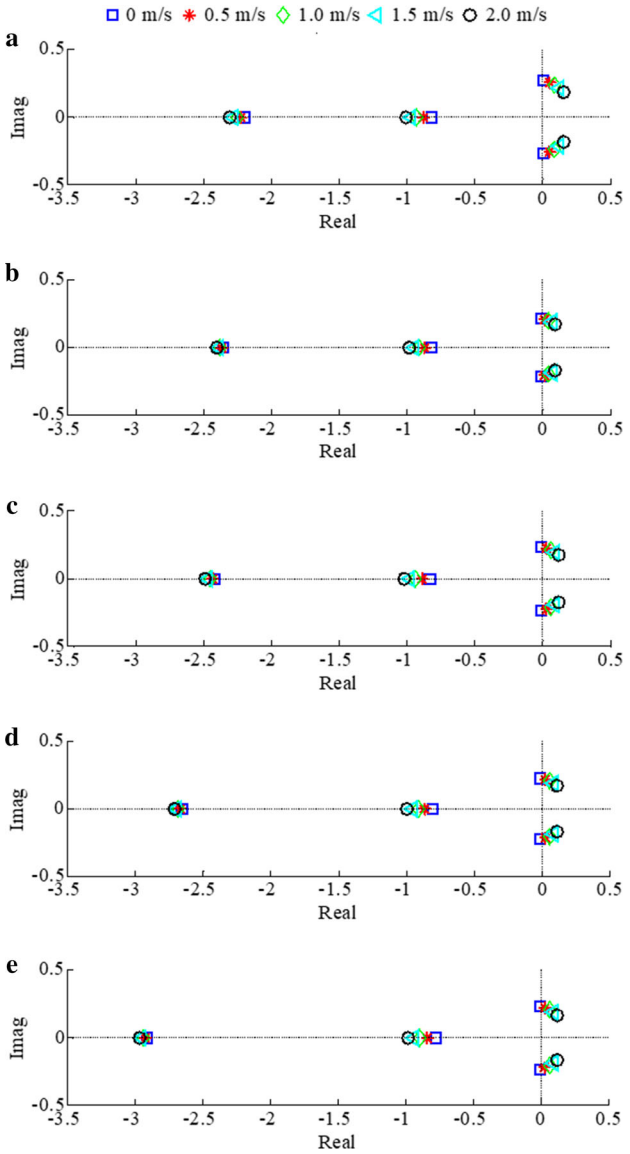

Fig. 18 Lateral eigenvalues with the stability derivative coefficients taken from ascending flight states at 0 m/s (**a**), 0.5 m/s (**b**), 1.0 m/s (**c**), 1.5 m/s (**d**) and 2.0 m/s (**e**)

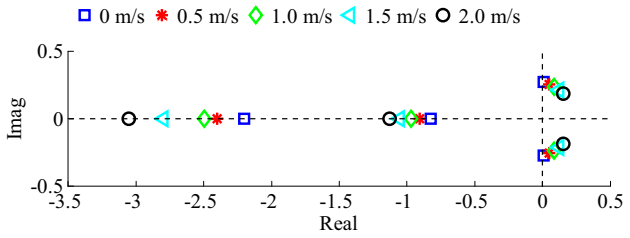

Fig. 19 Lateral eigenvalues when N_r^+ is allowed to vary with the ascending speed

of control algorithms that are applied to vertically ascending flight while considering the level of energy consumption.

Acknowledgement This work was supported by the Vietnam National Foundation for Science and Technology Development (NAFOSTED) (Grant 107.01-2018.05).

References

1. Willmott, A.P., Ellington, C.P.: The mechanics of flight in the hawkmoth Manduca sexta. I. Kinematics of hovering and forward flight. J. Exp. Biol. **200**, 2705–2722 (1997)
2. Willmott, A.P., Ellington, C.P.: The mechanics of flight in the hawkmoth Manduca sexta. II. Aerodynamic consequences of kinematic and morphological variation. J. Exp. Biol. **200**, 2723–2745 (1997)
3. Shyy, W., Aono, H., Chimakurthi, S.K., et al.: Recent progress in flapping wing aerodynamics and aeroelasticity. Prog. Aerosp. Sci. **46**, 284–327 (2010). https://doi.org/10.1016/j.paerosci.2010.01.001
4. Taha, H.E., Hajj, M.R., Nayfeh, A.H.: Flight dynamics and control of flapping-wing MAVs: a review. Nonlinear Dyn. **70**, 907–939 (2012). https://doi.org/10.1007/s11071-012-0529-5
5. Sun, M.: Insect flight dynamics: stability and control. Rev. Mod. Phys. **86**, 615–646 (2014). https://doi.org/10.1103/RevModPhys.86.615
6. Liu, H., Ravi, S., Kolomenskiy, D., et al.: Biomechanics and biomimetics in insect-inspired flight systems. Philos. Trans. R. Soc. B **371**, 20150390 (2016). https://doi.org/10.1098/rstb.2015.0390
7. Nakata, T., Noda, R., Kumagai, S., et al.: A simulation-based study on longitudinal gust response of flexible flapping wings. Acta. Mech. Sin. **34**, 1048–1060 (2018). https://doi.org/10.1007/s10409-018-0789-5
8. Muijres, F.T., Elzinga, M.J., Melis, J.M., et al.: Flies evade looming targets by executing rapid visually directed banked turns. Science **344**, 172–177 (2014). https://doi.org/10.1126/science.1248955
9. Shen, C., Sun, M.: Wing and body kinematics measurement and force analyses of landing in fruit flies. Bioinspirat. Biomimetics **13**, 016004 (2017). https://doi.org/10.1088/1748-3190/aa934b
10. Shen, C., Liu, Y., Sun, M.: Lift and power in fruitflies in vertically-ascending flight. Bioinspiration & biomimetics **13**, 056008 (2018). https://doi.org/10.1088/1748-3190/aad212
11. Xiong, Y., Sun, M.: Dynamic flight stability of a bumblebee in forward flight. Acta. Mech. Sin. **24**, 25–36 (2008). https://doi.org/10.1007/s10409-007-0121-2
12. Nguyen, A.T., Han, J.S., Han, J.H.: Effect of body aerodynamics on the dynamic flight stability of the hawkmoth Manduca sexta. Bioinspirat. Biomimetics **12**, 016007 (2016). https://doi.org/10.1088/1748-3190/12/1/016007
13. Liu, L., Sun, M.: Dynamic flight stability of hovering mosquitoes. J. Theor. Biol. **464**, 149–158 (2019). https://doi.org/10.1016/j.jtbi.2018.12.038
14. Au, L.T.K., Phan, V.H., Park, H.C.: Longitudinal flight dynamic analysis on vertical takeoff of a tailless flapping-wing micro air vehicle. J. Bionic Eng. **15**, 283–297 (2018). https://doi.org/10.1007/s42235-018-0022-z
15. Meng, X.G., Sun, M.: Wing and body kinematics of forward flight in drone-flies. Bioinspirat. Biomimetics **11**, 056002 (2016). https://doi.org/10.1088/1748-3190/11/5/056002
16. Warfvinge, K., KleinHeerenbrink, M., Hedenström, A.: The power–speed relationship is U-shaped in two free-flying hawkmoths (*Manduca sexta*). J. R. Soc. Interface **14**, 20170372 (2017). https://doi.org/10.1098/rsif.2017.0372

17. Kim, J.K., Han, J.S., Lee, J.S., Han, J.H.: Hovering and forward flight of the hawkmoth Manduca sexta: Trim search and 6-DOF dynamic stability characterization. Bioinspirat. Biomimetics **10**, 056012 (2015). https://doi.org/10.1088/1748-3190/10/5/056012
18. Nguyen, A.T., Tran, N.D., Vu, T.T., et al.: A neural-network-based approach to study the energy-optimal hovering wing kinematics of a bionic hawkmoth model. J. Bionic Eng. **16**, 904–915 (2019). https://doi.org/10.1007/s42235-019-0105-5
19. Berman, G.J., Wang, Z.J.: Energy-minimizing kinematics in hovering insect flight. J. Fluid Mech. **582**, 153–168 (2007). https://doi.org/10.1017/S0022112007006209
20. Ellington, C.P.: The aerodynamics of hovering insect flight. II. Morphological parameters. Philos. Trans. R. Soc. London **305**, 17–40 (1984). https://doi.org/10.1098/rstb.1984.0050
21. O'Hara, R.P., Palazotto, A.N.: The morphological characterization of the forewing of the Manduca sexta species for the application of biomimetic flapping wing micro air vehicles. Bioinspirat. Biomimetics **7**, 046011 (2012). https://doi.org/10.1088/1748-3182/7/4/046011
22. Sane, S.P., Dickinson, M.H.: The aerodynamic effects of wing rotation and a revised quasi-steady model of flapping flight. J. Exp. Biol. **205**, 1087–1096 (2002)
23. Lee, Y.J., Lua, K.B., Lim, T.T., et al.: A quasi-steady aerodynamic model for flapping flight with improved adaptability. Bioinspirat. Biomimetics **11**, 036005 (2016). https://doi.org/10.1088/1748-3190/11/3/036005
24. Casey, T.M.: A comparison of mechanical and energetic estimates of flight cost for hovering sphinx moths. J. Exp. Biol. **91**, 117–129 (1981)
25. Marquardt, D.W.: An algorithm for least-squares estimation of nonlinear parameters. J. Soc. Ind. Appl. Math. **11**, 431–441 (1963). https://doi.org/10.1137/0111030
26. Nguyen, A.T., Kim, J.K., Han, J.S., et al.: Extended unsteady vortex-lattice method for insect flapping wings. J. Aircraft **53**, 1709–1718 (2016). https://doi.org/10.2514/1.C033456
27. Nguyen, A.T., Han, J.H.: Wing flexibility effects on the flight performance of an insect-like flapping-wing micro-air vehicle. Aerosp. Sci. Technol. **79**, 468–481 (2018). https://doi.org/10.1016/j.ast.2018.06.007
28. Nguyen, A.T., Pham, T.D., Vu, Q.T.: Flapping flight in the wake of a leading insect. J. Mech. Sci. Technol. **33**, 3277–3288 (2019). https://doi.org/10.1007/s12206-019-0623-4
29. Nguyen, A.T., Han, J.H., Vu, T.T.: The effects of wing mass asymmetry on low-speed flight characteristics of an insect model. Int. J. Aeron. Space Sci. **20**, 940–952 (2019). https://doi.org/10.1007/s42405-019-00165-6
30. Ellington, C.P.: Aerodynamics and the origin of insect flight. Adv. Insect Physiol **23**, 171–210 (1991)
31. Ellington, C.P., Van Den Berg, C., Willmott, A.P., et al.: Leading-edge vortices in insect flight. Nature **384**, 626–630 (1996). https://doi.org/10.1038/384626a0
32. Ramasamy, M., Leishman, J.G.: A Reynolds number-based blade tip vortex model. J. Am. Helicopter Soc. **52**, 214–223 (2007). https://doi.org/10.4050/JAHS.52.214
33. Katz, J., Plotkin, A.: Low-speed aerodynamics: from wing theory to panel methods, 2nd edn. Cambridge University Press, New York (2001)
34. Liu, H., Aono, H.: Size effects on insect hovering aerodynamics: an integrated computational study. Bioinspirat. Biomimetics **4**, 015002 (2009). https://doi.org/10.1088/1748-3182/4/1/015002
35. Zheng, L., Hedrick, T.L., Mittal, R.: A multi-fidelity modelling approach for evaluation and optimization of wing stroke aerodynamics in flapping flight. J. Fluid Mech. **721**, 118–154 (2013). https://doi.org/10.1017/jfm.2013.46
36. Han, J.S., Kim, J.K., Chang, J.W., et al.: An improved quasi-steady aerodynamic model for insect wings that considers movement of the center of pressure. Bioinspirat. Biomimetics **10**, 046014 (2015). https://doi.org/10.1088/1748-3190/10/4/046014
37. Lagarias, J.C., Reeds, J.A., Wright, M.H., et al.: Convergence behavior of the Nelder-Mead simplex algorithm in low dimensions. SIAM J. Optim. **9**, 112–147 (1999). https://doi.org/10.1137/S1052623496303470
38. Mitchell, M.: An introduction to genetic algorithms. MIT Press, Massachusetts (1998)
39. Zhang, Y.L., Sun, M.: Dynamic flight stability of hovering model insects: theory versus simulation using equations of motion coupled with Navier–Stokes equations. Acta. Mech. Sin. **26**, 509–520 (2010). https://doi.org/10.1007/s10409-010-0360-5
40. Zhang, Y.L., Wu, J.H., Sun, M.: Lateral dynamic flight stability of hovering insects: theory vs numerical simulation. Acta Mechanica Sin. **28**, 221–231 (2012). https://doi.org/10.1007/s10409-012-0011-0
41. Etkin, B., Reid, L.D.: Dynamics of Flight: Stability and Control. Wiley, New York (1996)
42. Luo, G., Du, G., Sun, M.: Effects of stroke deviation on aerodynamic force production of a flapping wing. AIAA J. **56**, 25–35 (2018). https://doi.org/10.2514/1.J055739
43. Cheng, B., Deng, X.: Translational and rotational damping of flapping flight and its dynamics and stability at hovering. IEEE Trans. Rob. **27**, 849–864 (2011). https://doi.org/10.1109/TRO.2011.2156170
44. Roccia, B.A., Preidikman, S., Massa, J.C.: Modified unsteady vortex-lattice method to study flapping wings in hover flight. AIAA J. **51**, 2628–2642 (2013). https://doi.org/10.2514/1.J052262
45. Han, J.S., Chang, J.W., Kim, J.K., et al.: Role of trailing-edge vortices on the hawkmothlike flapping wing. J. Aircraft **52**, 1256–1266 (2015). https://doi.org/10.2514/1.C032768